Research Square

Preprints are preliminary reports that have not undergone peer review.
They should not be considered conclusive, used to inform clinical practice,
or referenced by the media as validated information.

A New Fluid-Structure Interaction Benchmark with an Analytical Solution Describing Vibration-Driven Propulsion in a Viscous Fluid

Vadim Anisimov

anisimov.vadim1996@gmail.com

Kazan Federal University

Artem Nuriev

Kazan Federal University

Olga Zaitseva

Kazan Federal University

Research Article

Keywords: Fluid–structure interaction, Benchmark problem, Analytical solution, Vibration-driven propulsion, Viscous flow, OpenFOAM

Posted Date: October 5th, 2026

DOI: https://doi.org/10.21203/rs.3.rs-10892297/v1

License: This work is licensed under a Creative Commons Attribution 4.0 International License.
Read Full License

Additional Declarations: No competing interests reported.

A New Fluid–Structure Interaction Benchmark with an Analytical Solution Describing Vibration-Driven Propulsion in a Viscous Fluid

Vadim Anisimov[1*], Artem Nuriev[1] and Olga Zaitseva[1]

[1*]Lobachevskii Institute of Mathematics and Mechanics, Kazan Federal University, Republic of Tatarstan, Russia.

*Corresponding author(s). E-mail(s): anisimov.vadim1996@gmail.com;
Contributing authors: 2anuriev@kpfu.ru; ONZajceva@kpfu.ru;

Abstract

This paper investigates the dynamics of a vibration-driven propulsion system in a fluid, modeled as a cylindrical vibration robot whose oscillations are induced by the movement of an internal mass. The system represents an attractive combination of bio-inspired physics and tractable mathematics.The directed motion of the system arises due to two-way fluid–structure interaction, mimicking the physics of a flapping wing. Despite the richness of the underlying physics, the problem admits an analytical solution with controlled accuracy, obtained in the paper using the method of asymptotic expansions. The solution explicitly describes the steady-state self-propulsion mode, determining the body oscillation amplitudes, phase shifts, and cruising speed through simple algebraic expressions. Finally, owing to the simple cylindrical geometry and the clear physical and mathematical foundation, the problem constitutes a convenient computational case for free-body motion in a viscous fluid. To capture the full system dynamics and validate the analytical framework, numerical simulations are performed in OpenFOAM using 3 and 2.5 degrees of freedom models. A comprehensive parametric study demonstrates good agreement between the numerical and analytical results: the average relative error for kinematics (oscillation amplitudes and phase shifts) does not exceed 2% (with average amplitude deviation about 3.5%), while the average deviation for the cruising speed is within 6%. Combining bio-inspired physics, a rigorous analytical solution, and modeling convenience makes the proposed problem a unique reference case for FSI calculations. The provided open-source configuration files and benchmark data offer a standardized test case for computational method development, code validation, and verification of numerical solvers.

Keywords: Fluid–structure interaction, Benchmark problem, Analytical solution, Vibration-driven propulsion, Viscous flow, OpenFOAM

1 Introduction

The development of numerical methods for modeling fluid–structure interaction (FSI) is an actively growing field in computational mechanics. Despite significant progress in algorithms and software, a key challenge remains the scarcity of benchmark problems that allow rigorous verification of numerical schemes and assessment of computational accuracy. This gap is particularly pronounced in the modeling of natural propulsors (fish, birds, insects) and bio-inspired propulsion systems, where two-way FSI coupling plays a crucial role.

Classical analytical theories of bio-inspired propulsion rely on inviscid flow models [1–7]. Such models qualitatively describe the key thrust-generation mechanisms; however, they do not provide accurate quantitative estimates of viscous interactions and thus cannot serve as benchmarks for numerical methods solving the full Navier–Stokes equations.

High-fidelity reproducible experimental measurements of live organisms and their artificial counterparts are also limited. The vast majority of laboratory studies [8–11] are conducted under forced oscillation conditions, where the propulsor kinematics are prescribed by a mechanical actuator. This allows detailed measurement of hydrodynamic loads but excludes (or significantly restricts) the feedback influence of the fluid on the motion, which is a key component of a complete FSI problem. Furthermore, experimental data inevitably contain measurement errors and are sensitive to specific setup conditions, making them difficult to use as strict benchmarks.

A promising platform for constructing analytical benchmarks is the asymptotic approach. Works [12–14] demonstrated its applicability to the problem of forced oscillations of a cylindrical wing in a viscous fluid. The resulting solution has a controllable error, governed by the order of the terms neglected in the asymptotic expansion. The broad applicability range of the results [12–14] has been confirmed by direct numerical simulations. However, these works do not describe the complete two-way coupling between the body and the fluid: the body kinematics remain prescribed rather than determined by the hydrodynamic interaction.

In the present work, the asymptotic solution is extended to a complete FSI system. We consider the dynamics of a self-propelled vibration-driven robot [15–19], which is a two-mass system consisting of a body and an internal mass. The robot body is a circular cylinder undergoing free translational and rotational oscillations in a viscous incompressible fluid under the action of internal and external hydrodynamic forces and moments. The internal forces and moments are generated by pendulum-like oscillations of the internal mass moving according to a prescribed law inside the body. An approximate analytical solution and a numerical solution of the problem are obtained.

The proposed problem possesses several features that make it a convenient FSI benchmark:

1. Simplicity of geometry. The cylindrical shape of the body allows analytical description of hydrodynamic fields in polar coordinates and minimizes computational costs in numerical implementation.
2. Natural FSI coupling. The body motion is not prescribed but is fully determined by the coupled solution of rigid-body dynamics and hydrodynamics. This provides complete two-way interaction, fundamentally distinguishing the problem from classical forced-oscillation formulations.
3. Bio-inspired analogy. The body oscillations generated by the internal mass motion produce thrust through the same mechanism as a flapping wing [12]. This makes the problem physically meaningful and connects it to a broad class of natural and artificial propulsive systems.
4. Existence of an analytical solution. Unlike the vast majority of FSI problems, the proposed formulation admits an approximate analytical solution that provides simple formulas for the cruising speed, translational and rotational oscillation amplitudes, and phase shifts between the body and internal mass oscillations.
5. Reproducibility. All elements of the problem statement, including geometry, internal mass motion law, and mechanical and hydrodynamic parameters, are fully defined and can be reproduced in any CFD package supporting FSI calculations.

The paper is organized as follows. Section 2 presents the problem statement: the mechanical model of the vibration-driven robot and the formulation of the hydrodynamic problem based on the Navier–Stokes equations. Section 3 is devoted to the derivation of the asymptotic analytical solution. Section 4 describes the numerical implementation in OpenFOAM. Section 5 presents the results of comparing the analytical and numerical solutions, error analysis, and discussion of the problem's applicability as a benchmark. Conclusions are summarized in the final section.

2 Problem Formulation

The system under consideration consists of a body of mass m_b with a cylindrical shell of radius a and a point internal mass m_im, as shown in Fig. 1. The total mass of the apparatus is $m_\mathrm{VR} = m_\mathrm{b} + m_\mathrm{im}$. Let $V_x(t)$, $V_y(t)$, $\Omega(t)$ denote the linear velocities of the body center and its angular velocity, $X(t)$, $Y(t)$ the coordinates of the internal mass in the coordinate system translating with the body center, and $F_x(t)$, $F_y(t)$, $M(t)$ the hydrodynamic forces and moment acting on the vibration-driven robot (VR).

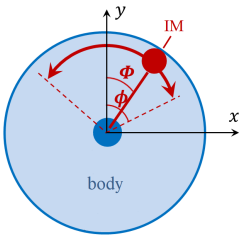


Fig. 1 Schematic of the VR. The body is shown in blue, the internal mass (IM) in red. The IM oscillates periodically about the y-axis with oscillation amplitude 2ϕ.

The internal mass performs pendulum-like oscillations in the xy-plane about the cylinder axis, with angular amplitude ϕ and frequency ω along a circular arc of maximum radius, so that its deviation from the y-direction is given by the time-dependent angle $\Phi(t)$. Its position is then determined by

$$X = a\sin\Phi, \quad Y = a\cos\Phi, \qquad \Phi(t) = \phi\cos\omega t.$$

The mechanical subsystem governing the motion of such a system is written as

$$\begin{aligned} I_{\mathrm{b}}\dot{\Omega} - m_{\mathrm{im}}a^2\ddot{\Phi} &= M + m_{\mathrm{im}}\left(Y\dot{V}_x - X\dot{V}_y\right), \\ m_{\mathrm{VR}}\dot{V}_x + m_{\mathrm{im}}\ddot{X} &= F_x, \\ m_{\mathrm{VR}}\dot{V}_y + m_{\mathrm{im}}\ddot{Y} &= F_y, \end{aligned} \tag{1}$$

where I_{b} is the moment of inertia of the body. The presence of the hydrodynamic force $\mathbf{F} = (F_x, F_y)$ and moment M on the right-hand side of (1) reflects the dynamic coupling conditions between the mechanical and hydrodynamic subproblems.

The external hydrodynamics is governed by the incompressible Navier–Stokes equations:

$$\frac{\partial\mathbf{u}}{\partial t} + (\mathbf{u}\cdot\nabla)\mathbf{u} = -\frac{1}{\rho}\nabla p + \nu\Delta\mathbf{u}, \qquad \nabla\cdot\mathbf{u} = 0, \tag{2}$$

where ρ is the fluid density and ν the kinematic viscosity.

On the VR body (the circular cylinder boundary C), kinematic coupling conditions are imposed; at infinity, undisturbed fluid conditions are applied:

$$\mathbf{u} = (V_x - a\Omega\sin\theta,\ V_y + a\Omega\cos\theta) \quad \text{on } C, \qquad \mathbf{u}\to 0 \quad \text{as } |\mathbf{x}|\to\infty, \tag{3}$$

where θ is the angular coordinate in the polar coordinate system translating with the body.

The hydrodynamic force and moment are expressed as surface integrals over the body boundary C:

$$F_x = \oint_C (\boldsymbol{\sigma}\cdot\mathbf{n})_x\, dl, \qquad F_y = \oint_C (\boldsymbol{\sigma}\cdot\mathbf{n})_y\, dl, \qquad M = \oint_C \left[\mathbf{r}\times(\boldsymbol{\sigma}\cdot\mathbf{n})\right]_z dl.$$

where $\mathbf{n}$ is the outward unit normal, $\mathbf{r}$ is the radius vector from the body center, and $\boldsymbol{\sigma}$ is the stress tensor:

$$\boldsymbol{\sigma} = -p\mathbf{I} + \boldsymbol{\tau}, \qquad \boldsymbol{\tau} = \mu\left(\nabla\mathbf{u} + (\nabla\mathbf{u})^{\mathsf{T}}\right),$$

with the dynamic viscosity $\mu = \rho\nu$.

The following assumptions are adopted for the subsequent solution:

$$\sin\Phi \approx \Phi, \quad \cos\Phi \approx 1, \tag{4}$$

$$m_{\mathrm{VR}} = \pi\rho a^2. \tag{5}$$

The first is the small-amplitude assumption for the internal mass oscillations ($\phi \ll 1$), and the second is the neutral buoyancy condition for the VR.

3 Approximate Analytical Solution

3.1 Asymptotic Model

We seek an approximate analytical solution to (1)–(5). We normalize X and Y by a, and the variables t, V, Ω, F, and M by

$$t_{\rm sc} = \omega^{-1}, \quad v_{\rm sc} = \frac{m_{\rm im}}{m_{\rm VR}} a\omega, \quad \omega_{\rm sc} = \frac{v_{\rm sc}}{a}, \quad f_{\rm sc} = \pi\rho a^2 v_{\rm sc}\omega, \quad m_{\rm sc} = a f_{\rm sc}.$$

Using assumptions (4) and (5), we rewrite (1) in dimensionless form:

$$\alpha\dot{\Omega} - \ddot{\Phi} = M + \gamma\dot{V}_x, \qquad \dot{V}_x + \ddot{\Phi} = F_x, \qquad \dot{V}_y = F_y, \tag{6}$$

where the dimensionless parameters are defined as

$$\gamma = \frac{m_{\rm im}}{m_{\rm VR}}, \qquad \alpha = \frac{m_{\rm b} r_{\rm b}^2}{m_{\rm VR} a^2} = (1-\gamma)\frac{r_{\rm b}^2}{a^2}.$$

We rewrite the Navier–Stokes equations (2) in terms of vorticity w and stream-function ψ in the moving polar coordinate system (r, θ) translating with the cylinder:

$$r > 1: \qquad w = \Delta\psi, \qquad \frac{\partial w}{\partial t} - \frac{\gamma}{r}\frac{\partial(\psi, w)}{\partial(r,\theta)} = \beta^{-1}\Delta w, \tag{7}$$

where $\beta = a^2\omega/\nu$ is the dimensionless frequency or Stokes parameter.

The boundary conditions (3) in the moving coordinate system become

$$r = 1: \quad \psi = 0, \quad \frac{\partial\psi}{\partial r} = -\Omega, \qquad r \to \infty: \quad \psi \sim rV_y\cos\theta - rV_x\sin\theta. \tag{8}$$

Assuming γ is a small parameter, we seek the coupled solution of the mechanical and hydrodynamic problems as series expansions in powers of γ, retaining the zeroth-order (denoted by superscript (0)) and first-order (superscript (1)) terms:

$$\psi = \psi^{(0)} + \gamma\psi^{(1)} + \cdots, \qquad w = w^{(0)} + \gamma w^{(1)} + \cdots.$$

The zeroth-order problem is

$$\frac{\partial w^{(0)}}{\partial t} - \beta^{-1}\Delta w^{(0)} = 0, \qquad w^{(0)} = \Delta\psi^{(0)},$$
$$r = 1: \quad \psi^{(0)} = 0, \quad \frac{\partial\psi^{(0)}}{\partial r} = -\Omega^{(0)}, \qquad r \to \infty: \quad \psi^{(0)} \sim -rV_x^{(0)}\sin\theta, \tag{9}$$

$$\alpha\dot{\Omega}^{(0)} - \ddot{\Phi} = M^{(0)}, \qquad \dot{V}_x^{(0)} + \ddot{\Phi} = F_x^{(0)}.$$

Its solution describes purely oscillatory motion of the VR.

The first-order solution comprises both steady and unsteady contributions. We consider only the steady part, which is obtained from the following problem:

$$-\beta^{-1}\Delta\langle w^{(1)}\rangle = \langle G\rangle, \qquad \langle w^{(1)}\rangle = \Delta\langle\psi^{(1)}\rangle, \qquad G = \frac{1}{r}\frac{\partial(\psi^{(0)}, w^{(0)})}{\partial(r,\theta)},$$
$$r = 1: \quad \langle\psi^{(1)}\rangle = \frac{\partial\langle\psi^{(1)}\rangle}{\partial r} = 0, \qquad r \to \infty: \quad \langle\psi^{(1)}\rangle \sim r\langle V_y^{(1)}\rangle\cos\theta, \tag{10}$$
$$\langle F_y^{(1)}\rangle = 0.$$

System (10) describes the steady-state motion when the time-averaged hydrodynamic force is zero. Its solution determines the cruising speed $\langle V_y\rangle \approx \gamma\langle V_y^{(1)}\rangle$.

Let

$$\Omega^{(0)} = \operatorname{Re}\left(\omega_0 e^{it}\right), \quad V^{(0)} = \operatorname{Re}\left(v_0 e^{it}\right), \qquad M^{(0)} = \operatorname{Re}\left(m_0 e^{it}\right), \quad F^{(0)} = \operatorname{Re}\left(f_0 e^{it}\right).$$

Using the linearity of (9), the solution of the hydrodynamic subproblem is

$$\psi^{(0)} = -\operatorname{Re}\left(\omega_0\psi_\Omega(r)e^{it}\right) - \sin\theta\,\operatorname{Re}\left(v_0\psi_V(r)e^{it}\right). \tag{11}$$

With $z = \sqrt{i\beta}$, the functions ψ_Ω, w_Ω, ψ_V, and w_V are expressed in terms of modified Bessel functions K_j [13, 20]:

$$\psi_\Omega = s_\Omega + \frac{w_\Omega}{z^2}, \qquad w_\Omega = -z\frac{K_0(zr)}{K_1(z)}, \quad s_\Omega = \frac{K_0(z)}{zK_1(z)}, \tag{12}$$
$$\psi_V = r - \frac{1}{r} - \frac{s_V}{r} + \frac{1}{z^2}w_V, \qquad w_V = z\frac{2K_1(zr)}{K_0(z)}, \quad s_V = \frac{2K_1(z)}{zK_0(z)}.$$

The branch cut for the square root is taken along the negative real axis so that $\sqrt{i\beta} = e^{i\pi/4}\sqrt{\beta}$.

Computing the force characteristics of the oscillating cylinder through the vorticity and its normal derivative on the cylinder surface [13], we obtain

$$m_0 = -i\omega_0\left(-\frac{4i}{\beta} + 2s_\Omega\right), \qquad f_0 = -iv_0(1 + 2s_V). \tag{13}$$

Substituting (13) into the mechanical subsystem in (9) yields

$$v_0 = -\frac{i\phi}{2(1+s_V)}, \qquad \omega_0 = -\frac{i\phi}{\alpha + 2s_\Omega - 4i/\beta}. \tag{14}$$

Equations (12)–(14) completely determine the leading-order solution.

We now solve the first-order problem (10). The function G and its solutions contain two azimuthal harmonics: $\cos\theta$ and $\sin 2\theta$. The latter does not contribute to either the force or the moment and is not needed for the calculation of $\langle V_y \rangle$. Retaining only the $\cos\theta$ harmonic in $\langle G \rangle$, we write

$$\langle G \rangle = \cos\theta\, \phi^2 G_1(r;\alpha,\beta), \qquad G_1 = \frac{1}{2r}\,\mathrm{Re}\left(\frac{\overline{w}_V \cdot \psi'_\Omega - \overline{\psi}_V \cdot w'_\Omega}{2(1+\overline{s}_V)(\alpha + 2s_\Omega - 4i/\beta)}\right),$$

where the overbar denotes complex conjugation and the prime denotes differentiation with respect to r.

We extract the spatial part of G_1 as

$$\widetilde{G}_1(r;\beta) = \frac{\overline{w}_V \cdot \psi'_\Omega - \overline{\psi}_V \cdot w'_\Omega}{2r},$$

and solve the following problem for Ψ:

$$\mathcal{L}_1 W = -\widetilde{G}_1, \qquad W = \mathcal{L}_1 \Psi, \qquad \Psi(1) = \Psi'(1) = 0, \qquad \Psi|_{r\to\infty} \sim \tilde{V} r.$$

The quantity $\tilde{V}$ is determined from the zero-mean-force condition, which, in terms of W, reads

$$W'(1) - W(1) = 0.$$

The solution to the above problem was obtained in [13]. Here we present the explicit expression for the cruising speed component:

$$\widetilde{V} = -\frac{\beta}{8}\int_1^\infty \widetilde{G}_1(r;\beta)(2r^2 \ln r - r^2 + 1)\, dr.$$

Once the complex quantity $\widetilde{V}$ is found, the cruising speed of the VR is computed as

$$\langle V_y \rangle \approx \gamma \langle V_y^{(1)} \rangle = \gamma \frac{\phi^2}{2|A|^2|\alpha + B|^2}\left(\alpha\,\mathrm{Re}(\widetilde{V}A) + \mathrm{Re}(\widetilde{V}B)\right), \tag{15}$$

where

$$A = 1 + s_V, \qquad B = 2s_\Omega + \frac{4i}{\beta}.$$

3.2 Final Analytical Formulas

From the derived solution, we extract the key dimensionless characteristics commonly used to quantify the motion of biomimetic propulsive systems: these include the kinematic parameters, i.e., the translational and rotational oscillation amplitudes κ and Θ, and the phase shifts φ_V and φ_Ω, as well as the propulsive characteristics, namely the dimensionless cruising speed u_{st}, the Strouhal number St, and the Reynolds number Re:

$$\kappa = \frac{A}{a}, \qquad u_{st} = \frac{U_{st}}{A\omega}, \qquad St = \frac{1}{\pi u_{st}}, \qquad Re = u_{st}\kappa\beta,$$

where A is the dimensional translational oscillation amplitude and U_{st} is the dimensional cruising speed. All quantities are expressed as functions of β, ϕ, γ, and α.

The dimensionless oscillation amplitudes are obtained from (14):

$$\kappa = \gamma|v_0| = \frac{\gamma\phi}{2|1+s_V|} = \frac{\gamma\phi}{|a_V|}, \qquad \Theta = \gamma|\omega_0| = \frac{\gamma\phi}{|\alpha + 2s_\Omega - 4i/\beta|} = \frac{\gamma\phi}{|a_\Omega|}. \tag{16}$$

The complex functions a_V and a_Ω can be computed via the Bessel functions (12) or, with an accuracy of 2% for $\beta > 50$, using the following asymptotic expansions:

$$a_V = 2(1+s_V) \approx 2 + \frac{4}{\sqrt{i\beta}} + \frac{2}{i\beta}, \qquad a_\Omega = \alpha + 2s_\Omega - \frac{4i}{\beta} \approx \alpha + \frac{2}{\sqrt{i\beta}} + \frac{3}{i\beta}. \tag{17}$$

The phase shifts between the body oscillations and the internal mass oscillations are

$$\varphi_V = \arccos\left(-\frac{\operatorname{Re} a_V}{|a_V|}\right), \qquad \varphi_\Omega = \arccos\left(-\frac{\operatorname{Re} a_\Omega}{|a_\Omega|}\right). \tag{18}$$

The dimensionless cruising speed u_{st} is related to $\langle V_y \rangle$ by $u_{st} = \langle V_y \rangle \gamma \kappa^{-1}$. It can be computed using (15) or approximated by

$$u_{st} \approx 0.5 \frac{\phi^2\gamma^2}{\alpha\kappa} \frac{\beta\alpha - 5.5\sqrt{\beta\alpha}}{1.33(\beta\alpha) + 12.7\sqrt{\beta\alpha} + 80.7}. \tag{19}$$

This approximation matches the universal asymptotics at large β, passes through zero at the chosen point, and has the correct extremum magnitude for small β.

4 Numerical Solution

4.1 Numerical Model

The numerical solution of (1)–(5) is performed for fixed mechanical parameters $\gamma = 0.6$ and $\alpha = 1 - \gamma = 0.4$, which ensure a pronounced response of the body to the internal mass oscillations, over the ranges $\beta \in [500, 4000]$ and $\phi \in [0.2, 0.85]$. The problem is discretized using the finite volume method in OpenFOAM [21].The simulations are performed in a bounded domain with the outer boundary located at a distance of $15a$ from the cylinder center. The domain size is chosen to minimize the influence of boundary conditions on the hydrodynamic forces acting on the VR.

The computational domain is discretized using a structured mesh generated by conformal mapping of a rectangular domain to the exterior of the circle (see Fig. 2a). The mesh is extruded in the spanwise direction with a single cell layer, as is standard for two-dimensional simulations in OpenFOAM. To increase resolution near the boundary layer, the mesh is exponentially refined in the radial direction (see Fig. 2b). The standard mesh size for all test cases is $N_{\text{cells}} = 2.5 \times 10^5$. The results of the mesh convergence study are presented in Section 4.2.

The discrete velocity and pressure values are stored at cell centers. The Gauss integration scheme is used for volume integrals. Pressure gradient approximation uses

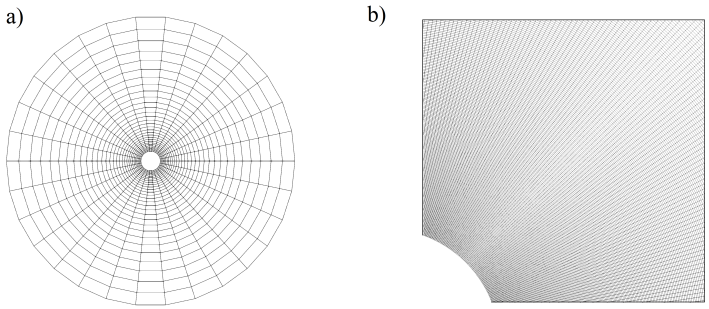


Fig. 2 (a) Typical mesh structure in the computational domain (coarse mesh shown); (b) Mesh structure near the cylinder with $N_{\text{cells}} = 2.5 \times 10^5$ cells.

linear interpolation. In the diffusion terms, Laplacian discretization employs a second-order symmetric scheme.

For interpolation of variables in the convective terms, the limited linear TVD scheme is used. Time discretization of the hydrodynamic subproblem is performed using the second-order Crank–Nicolson implicit scheme.

The discretized system is solved using the PIMPLE method. The pressure equation is solved using the preconditioned conjugate gradient method (PCG) with the geometric-algebraic multi-grid (GAMG) preconditioner. The velocity components are solved using the preconditioned bi-conjugate gradient method (PBiCG) with the DILU preconditioner.

Two motion regimes are considered: (i) the free regime, where the VR has three degrees of freedom (3DOF); and (ii) the cruising regime, where the VR can freely rotate and oscillate along the x-axis but moves at a constant cruising speed along the y-axis (2.5DOF).

The free motion of the VR in the fluid is modeled using the sixDoFRigidBodyMotion OpenFOAM library. The mechanical subsystem equations are integrated using the second-order Newmark implicit scheme with parameters $\gamma^* = 0.5$ and $\beta^* = 0.25$. A custom class externalForce was developed to model the forces and moments on the VR due to the internal mass motion.

For the cruising regime (2.5DOF), the secant method is used to determine the cruising speed. A custom library UpdateBC was implemented as a functionObject in OpenFOAM.

To ensure full reproducibility, all libraries and the complete case setup are provided in a public repository [22].

4.2 Verification

To ensure the correctness of the numerical simulations and to estimate discretization errors, calculations were performed on four successively refined meshes. The mesh parameters are specified by the number of nodes in the radial (N_r) and tangential (N_θ) directions: $N_r \times N_\theta = 330 \times 330$, 410×410, 500×500, and 610×610, corresponding to total cell counts from 1.09×10^5 to 3.72×10^5. The study was conducted for two

regimes: $\beta = 1000$, $\phi = 0.85$, $\gamma = 0.6$ (moderate frequency, maximum amplitude) and $\beta = 3000$, $\phi = 0.4$, $\gamma = 0.6$ (high frequency, moderate amplitude). This allows assessment of the influence of parameters on both numerical convergence and the applicability range of the asymptotic model.

The finest mesh 610×610 is taken as the reference for convergence assessment. The relative error err for each quantity on coarser meshes is computed relative to the finest mesh. A comparison of mesh parameters and results is presented in Table 1.

Table 1 Mesh convergence analysis

	$N_r \times N_\theta$				Analytical
	330×330	410×410	500×500	610×610	solution
			$\beta = 1000$, $\phi = 0.85$, $\gamma = 0.6$		
N_{cells}	1.09×10^5	1.68×10^5	2.50×10^5	3.72×10^5	–
u_{st}	0.4511	0.4542	0.4561	0.4573	0.4461
err, %	−1.36	−0.68	−0.26	–	–
κ	0.2375	0.2375	0.2375	0.2375	0.2439
err, %	0.00	0.00	0.00	–	–
Θ	1.089	1.088	1.088	1.088	1.140
err, %	+0.09	0.00	0.00	–	–
			$\beta = 3000$, $\phi = 0.4$, $\gamma = 0.6$		
N_{cells}	1.09×10^5	1.68×10^5	2.50×10^5	3.72×10^5	–
u_{st}	0.2619	0.2678	0.2706	0.2726	0.2936
err, %	−3.92	−1.76	−0.73	–	–
κ	0.1148	0.1141	0.1141	0.1141	0.1169
err, %	+0.61	0.00	0.00	–	–
Θ	0.5369	0.5365	0.5364	0.5362	0.5625
err, %	+0.13	+0.06	+0.04	–	–

The data demonstrate monotonic convergence of all quantities with mesh refinement. The cruising speed u_{st} is the most sensitive to discretization. From the coarsest mesh (330×330) to the finest (610×610), the change in u_{st} is about 1.4% for $\beta = 1000$ and about 4% for $\beta = 3000$, with the error on the 500×500 mesh relative to the finest not exceeding 0.8%.

The oscillation amplitudes κ and Θ show practical independence from mesh resolution even on coarse grids. This indicates that kinematic characteristics are correctly reproduced even on relatively coarse meshes.

In addition to convergence assessment, Table 1 allows a preliminary comparison of the numerical results with the asymptotic theory predictions. Good qualitative and quantitative agreement is observed for all investigated regimes. The relative difference between the analytical prediction and the numerical solution on the finest mesh for the oscillation amplitudes κ and Θ is 2.5–4.7%, and for the cruising speed u_{st} is 2.5–7.2%.

Based on the mesh convergence analysis, the $N_r \times N_\theta = 500 \times 500$ mesh was selected for the subsequent verification calculations, providing an optimal balance between accuracy and computational cost.

5 Numerical Results

5.1 Free Motion of the VR (3DOF Regime)

To analyze the physical realizability of the cruising regime predicted by the asymptotic theory, we consider the startup of the vibration robot from rest.

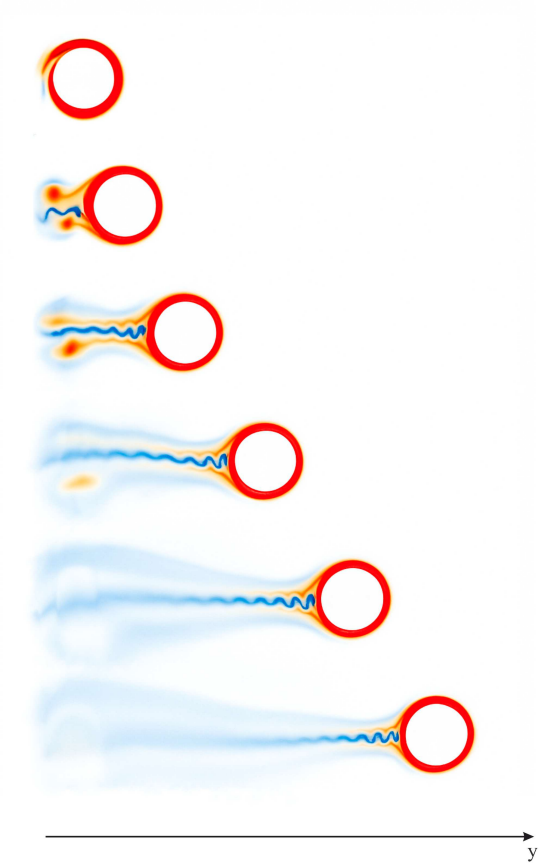


Fig. 3 Free motion of the VR for $\beta = 1000$, $\phi = 0.85$, $\gamma = 0.6$ at times $t = 10, 40, 70, 100, 130$ (from top to bottom). The oscillation period is $T \approx 3.77$. The vorticity field shows the formation of the vortex structure during the transition to the cruising regime.

Figure 3 presents instantaneous vorticity fields at various times for $\beta = 1000$, $\phi = 0.85$, $\gamma = 0.6$, illustrating the startup process. The flow visualization reveals the formation of the hydrodynamic structure responsible for self-propulsion. The body

oscillations induced by the internal mass motion generate an oscillatory flow in the surrounding fluid. The nonlinear interaction of oscillations leads to the appearance of a steady jet near the body: the fluid is ejected backward with increased velocity, creating thrust by momentum conservation. This mechanism underlies the motion of a wide class of bio-inspired devices and is also the primary mechanism for living organisms, such as fish, insects, and birds, that employ oscillatory or undulatory body movements for propulsion.

Secondary jet flow forms gradually. At the initial stage (Fig. 3, $t = 10$), the vortex structure is nearly symmetric, and the mean velocity of the robot is close to zero. As the motion develops ($t = 40$, 70, 100), an asymmetric vortex wake begins to form, corresponding to the emergence of the jet flow, and the robot gains speed (in the direction of the y-axis). At $t = 130$, the flow structure is nearly fully developed, indicating that the system is close to the cruising regime.

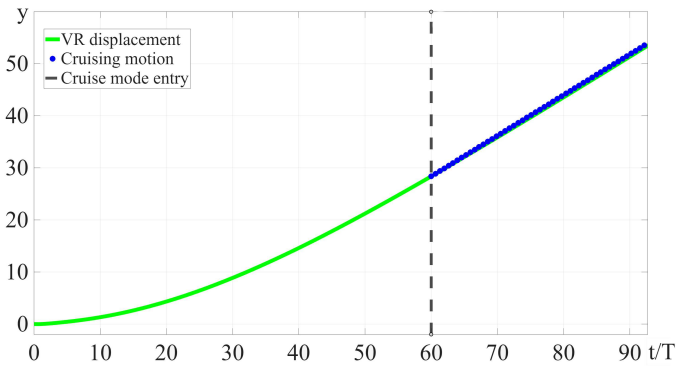


Fig. 4 Displacement of the VR along the y-axis versus time. $\beta = 2000$, $\phi = 0.85$, $\gamma = 0.6$.

Figure 4 shows the VR displacement along the y-axis for $\beta = 2000$, $\phi = 0.85$, $\gamma = 0.6$. The transition to the cruising regime is manifested by the linear dependence $y(t)$ after the transient process, corresponding to motion at a constant mean speed along y. The cruising speed can be determined from the slope of the linear segment, which is marked by the dashed line. Quantitative values of the VR speed at various times are given in Table 2.

Figure 5 presents the time histories of the body rotation angle and the translational motion of the VR center of mass along the x-axis. At startup ($t = 0$), the internal mass has maximum acceleration, creating an initial impulse transmitted to the body. As a result, the body shifts in the positive x direction and rotates counterclockwise.

However, in contrast to a simple inertial response, which would return the body to its initial position during the reverse motion of the internal mass, the system exhibits more complex dynamics: the body does not return, because the history-dependent hydrodynamic force (the Basset force) comes into play. Consequently, the mean force along y remains non-zero for several periods (in Fig. 4, up to $t/T \approx 10$), displacing

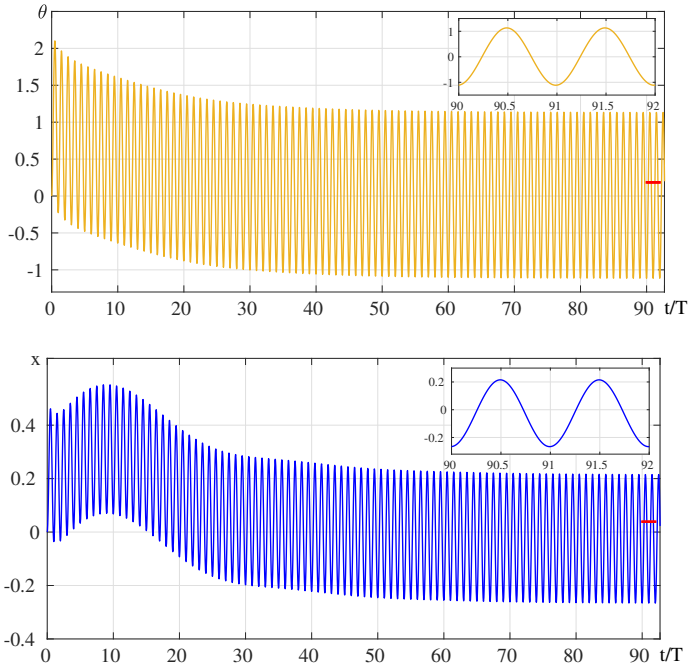


Fig. 5 Time histories of the VR rotation angle (top) and the center-of-mass translational motion along the x-axis (bottom). $\beta = 2000$, $\phi = 0.85$, $\gamma = 0.6$.

the body from $x = 0$ (the consequences of the initial impulse are visible at the end of the vortex wake in Fig. 4).

After startup, the body acquires a non-zero mean angular velocity (clockwise). Combined with the motion along y, this generates an additional hydrodynamic force (the Magnus force) acting along x. This force tends to return the body toward $x = 0$. After $t/T \approx 10$, this force becomes dominant and the body begins to return toward $x = 0$.

Figure 6 shows the phase shifts between the body oscillations and the internal mass oscillations for $\beta = 3000$, $\phi = 0.85$, $\gamma = 0.6$. In the steady state, both translational and rotational phase shifts are nearly π relative to the internal mass oscillations, i.e., the body moves almost in antiphase with the internal mass. This is fully consistent with the predictions of the asymptotic theory (17).

Table 2 provides detailed quantitative information on the transient dynamics for various values of β. For each β, the period-averaged speed u_{st}, amplitudes κ and Θ, and phase shifts φ_V and φ_Ω are given at different times normalized by the oscillation period T. The last row for each β shows the asymptotic values.

Table 2 Transient dynamics and comparison with the analytical solution for $\phi = 0.85$, $\gamma = 0.6$

β	t/T	u_{st}	κ	Θ	φ_V/π	φ_Ω/π
500	10	0.1549	0.2340	1.0466	0.9762	0.9560
	30	0.2923	0.2342	1.0417	0.9762	0.9549
	50	0.3478	0.2336	1.0412	0.9756	0.9555
	70	0.3631	0.2336	1.0411	0.9762	0.9555
	90	0.3670	0.2336	1.0411	0.9756	0.9549
	Analytical	0.3154	0.2394	1.0888	0.9805	0.9528
1000	10	0.1559	0.2384	1.0951	0.9825	0.9687
	30	0.3391	0.2383	1.0894	0.9825	0.9682
	50	0.4223	0.2378	1.0884	0.9825	0.9682
	70	0.4487	0.2376	1.0882	0.9825	0.9682
	90	0.4564	0.2376	1.0882	0.9822	0.9677
	Analytical	0.4461	0.2439	1.1402	0.9861	0.9660
2000	10	0.1396	0.2417	1.1305	0.9888	0.9782
	30	0.3366	0.2417	1.1251	0.9888	0.9772
	50	0.4523	0.2410	1.1236	0.9883	0.9772
	70	0.5003	0.2407	1.1232	0.9883	0.9772
	90	0.5175	0.2406	1.1230	0.9878	0.9767
	Analytical	0.5639	0.2471	1.1781	0.9901	0.9756
3000	10	0.1221	0.2432	1.1464	0.9905	0.9825
	30	0.3043	0.2434	1.1416	0.9905	0.9815
	50	0.4369	0.2427	1.1398	0.9899	0.9815
	70	0.5057	0.2422	1.1392	0.9894	0.9815
	90	0.5350	0.2420	1.1390	0.9889	0.9809
	Analytical	0.6240	0.2485	1.1953	0.9919	0.9800
4000	10	0.1056	0.2438	1.1553	0.9915	0.9846
	30	0.2572	0.2448	1.1514	0.9918	0.9841
	50	0.3932	0.2438	1.1496	0.9910	0.9836
	70	0.4852	0.2432	1.1489	0.9905	0.9836
	90	0.5321	0.2429	1.1486	0.9899	0.9831
	Analytical	0.6623	0.2494	1.2057	0.9929	0.9826

5.2 Cruising Motion (2.5DOF Regime)

For a detailed study of the steady-state motion, the 2.5DOF regime was used, where the VR can freely rotate and oscillate along the x-axis but moves at a constant cruising speed along the y-axis.

Figures 7 and 8 show the translational κ and rotational Θ oscillation amplitudes as functions of β for various internal mass oscillation amplitudes ϕ at fixed $\gamma = 0.6$. The dashed lines correspond to the analytical solution, and the markers show the numerical results. The numerically obtained amplitudes κ and Θ agree with the theoretical predictions with high accuracy over the entire ϕ and β ranges. The relative

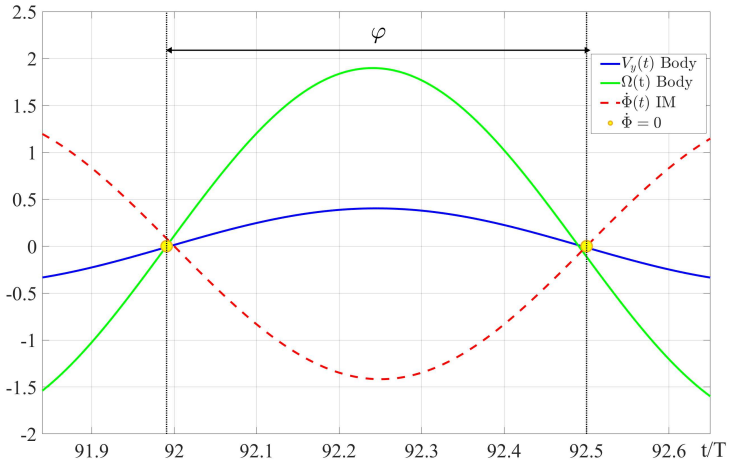


Fig. 6 Phase shifts between the VR body oscillations and the internal mass oscillations for $\beta = 3000$, $\phi = 0.85$, $\gamma = 0.6$.

error for κ is at most 3.2%, and for Θ at most 4.8% (see Table 3). It is also worth noting that as β increases, the oscillation amplitudes κ and Θ approach constant values, which is exactly consistent with the asymptotic theory predictions.

Figure 9 shows the cruising speed u_{st} as a function of β for various ϕ at $\gamma = 0.6$. The corresponding data are also given in Table 3.

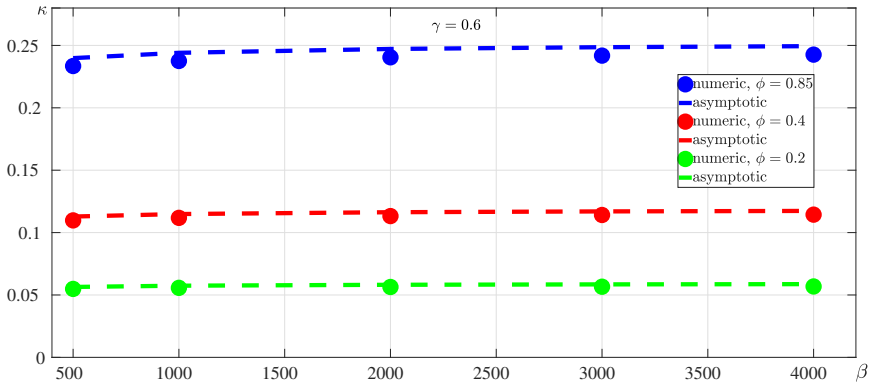


Fig. 7 Translational oscillation amplitude κ versus dimensionless frequency β for various internal mass oscillation amplitudes ϕ at fixed γ.

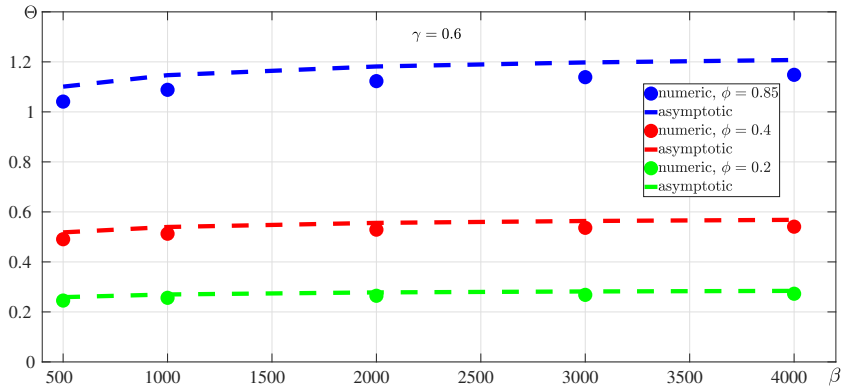


Fig. 8 Rotational oscillation amplitude Θ versus dimensionless frequency β for various internal mass oscillation amplitudes ϕ at fixed γ.

Table 3 VR motion characteristics in the cruising regime. Superscript $*$ denotes numerical results.

β	u_{st}			κ			Θ			φ_V/π			φ_Ω/π		
	u_{st}^*	u_{st}	err,%	κ^*	κ	err,%	Θ^*	Θ	err,%	φ_V^*/π	φ_V/π	err,%	φ_Ω^*/π	φ_Ω/π	err,%
							$\phi = 0.85$, $\gamma = 0.6$								
500	0.3649	0.3154	-15.69	0.2335	0.2394	2.46	1.0412	1.0888	4.37	0.9761	0.9805	0.45	0.9554	0.9528	-0.28
1000	0.4561	0.4461	-2.24	0.2375	0.2439	2.60	1.0883	1.1402	4.56	0.9825	0.9861	0.36	0.9682	0.9660	-0.22
2000	0.5239	0.5639	7.09	0.2405	0.2471	2.68	1.1230	1.1781	4.68	0.9872	0.9901	0.29	0.9772	0.9756	-0.16
3000	0.5513	0.6240	11.65	0.2418	0.2485	2.68	1.1388	1.1953	4.73	0.9894	0.9919	0.25	0.9814	0.9800	-0.14
4000	0.5688	0.6623	14.12	0.2426	0.2494	2.71	1.1482	1.2057	4.77	0.9904	0.9929	0.26	0.9830	0.9826	0.03
							$\phi = 0.4$, $\gamma = 0.6$								
500	0.1612	0.1484	-8.58	0.1098	0.1127	2.55	0.4907	0.5124	4.24	0.9804	0.9805	0.01	0.9575	0.9528	-0.28
1000	0.2043	0.2099	2.69	0.1118	0.1148	2.57	0.5127	0.5366	4.45	0.9857	0.9861	0.04	0.9676	0.9660	-0.17
2000	0.2519	0.2654	5.07	0.1132	0.1163	2.60	0.5290	0.5544	4.58	0.9899	0.9901	0.02	0.9772	0.9756	-0.16
3000	0.2706	0.2936	7.83	0.1141	0.1169	2.42	0.5364	0.5625	4.65	0.9915	0.9919	0.04	0.9814	0.9800	-0.15
4000	0.2871	0.3117	7.88	0.1144	0.1173	2.52	0.5409	0.5674	4.67	0.9925	0.9929	0.04	0.9835	0.9826	-0.09
							$\phi = 0.2$, $\gamma = 0.6$								
500	0.0739	0.0742	0.47	0.0549	0.0563	2.55	0.2454	0.2562	4.21	0.9809	0.9805	-0.04	0.9549	0.9528	-0.22
1000	0.1064	0.1050	-1.33	0.0558	0.0574	2.70	0.2564	0.2683	4.43	0.9867	0.9861	-0.06	0.9676	0.9660	-0.17
2000	0.1287	0.1327	3.01	0.0564	0.0581	3.02	0.2646	0.2772	4.55	0.9910	0.9901	-0.09	0.9772	0.9756	-0.16
3000	0.1439	0.1468	2.01	0.0566	0.0585	3.15	0.2682	0.2813	4.64	0.9931	0.9919	-0.12	0.9809	0.9800	-0.09
4000	0.1583	0.1558	-1.6	0.0578	0.0587	1.56	0.2727	0.2837	3.86	0.9925	0.9930	0.04	0.9830	0.9826	-0.04

As seen from Fig. 9 and Table 3, the differences between the approximate analytical prediction and the numerical data for the cruising speed are on average larger than for the body oscillation amplitudes and depend on both β and ϕ.

For small amplitudes ($\phi = 0.2$), the error is minimal and does not exceed 3% over the entire frequency range, with no systematic dependence on β and fluctuations near zero. This indicates that for such small perturbations, we have reached the limit of

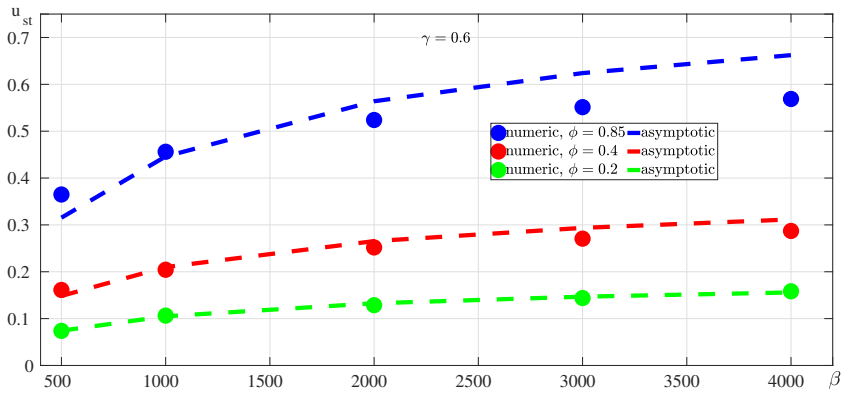


Fig. 9 Cruising speed u_{st} versus dimensionless frequency β for various internal mass oscillation amplitudes ϕ at fixed γ.

numerical accuracy in determining the cruising speed, due to the difficulty of accurately computing the hydrodynamic force balance in the small-ϕ limit. In this regime, the asymptotic theory appears to give a virtually exact solution, and the observed deviations are due exclusively to numerical errors in determining the mean force.

As ϕ increases (and, consequently, the body oscillation amplitudes increase), the error in the asymptotic prediction of u_{st} grows, which is associated with the strengthening of nonlinear effects not accounted for in the two-term asymptotic expansion. For $\phi = 0.4$, the relative error ranges from -8.58% at $\beta = 500$ to $+7.88\%$ at $\beta = 4000$; for the maximum considered amplitude $\phi = 0.85$, the error increases to -15.69% at $\beta = 500$ and $+14.12\%$ at $\beta = 4000$. The best agreement is achieved in the intermediate frequency range ($\beta \approx 1000$–2000), where the relative error for $\phi = 0.85$ is only -2.24% at $\beta = 1000$, and for $\phi = 0.4$ is $+2.69\%$ at $\beta = 1000$.

Qualitative comparison of the secondary flow patterns presented in Fig. 10 for $\beta = 500$ and 5000 shows that the constructed numerical and analytical solutions not only yield close integral characteristics of the VR motion but also identically describe the flow structure over the entire investigated parameter range.

Table 4 presents the Reynolds numbers Re and Strouhal numbers St for all performed calculations. These parameters are universal dimensionless similarity criteria for propulsive systems and are widely used in the classification of bio-inspired motion regimes. It should be noted that at maximum values of β and ϕ, the Strouhal number reaches values $St \approx 0.48$–0.51, which is close to the characteristic range $St \approx 0.2$–0.4 of natural locomotion systems, including swimming fish, flying insects, and birds [6, 23, 24].

6 Conclusions

This paper has presented the simplest self-propelled system, a cylindrical vibration robot whose oscillations are induced by internal mass motion, with directed motion

Table 4 Numerical and analytical values of Reynolds number Re and Strouhal number St for the VR cruising regime. Superscript $*$ denotes numerical results.

β	Re*	Re	St*	St
$\gamma = 0.6$, $\phi = 0.85$				
500	42.600	37.750	0.872	1.009
1000	108.330	108.780	0.698	0.713
2000	251.960	278.630	0.608	0.564
3000	399.890	465.190	0.577	0.510
4000	552.080	660.780	0.560	0.481
$\gamma = 0.6$, $\phi = 0.4$				
500	8.845	8.360	1.975	2.145
1000	22.841	24.091	1.558	1.516
2000	57.052	61.705	1.264	1.200
3000	92.647	103.016	1.176	1.084
4000	131.361	146.296	1.109	1.021
$\gamma = 0.6$, $\phi = 0.2$				
500	2.027	2.090	4.310	4.289
1000	5.938	6.023	2.993	3.032
2000	14.510	15.426	2.474	2.399
3000	24.441	25.754	2.212	2.168
4000	36.577	36.573	2.011	2.043

arising from two-way interaction with the surrounding fluid. The key bio-inspired mechanisms of this interaction have been revealed through asymptotic and numerical solutions. As noted in the Introduction, the combination of features of the proposed problem makes it a convenient tool for testing and debugging numerical methods, verifying FSI algorithms, and assessing the accuracy of various coupling schemes. The conducted study confirms each of these features.

1. Simplicity of geometry. The cylindrical body shape made it possible to obtain an analytical solution in polar coordinates, while in the numerical implementation a structured orthogonal mesh, generated by conformal mapping, provided high accuracy at moderate computational cost.
2. Natural FSI coupling. In the developed models, the body motion is fully determined by the coupled solution of rigid-body dynamics and hydrodynamics. It is the two-way FSI coupling that determines all key motion characteristics: the oscillation amplitudes and frequencies, the phase shifts between body and internal mass oscillations, and the cruising speed.
3. Bio-inspired analogy.The analytical solution and numerical simulations show that the body oscillations generated by the internal mass motion produce thrust through the formation of a secondary jet, a mechanism analogous to that of a flapping wing. At maximum β and ϕ, the Strouhal number reaches values $St \approx 0.48$–0.51, which is close to the range characteristic of natural locomotion systems.
4. Existence of an analytical solution. An approximate analytical solution has been constructed using the method of asymptotic expansions, providing simple formulas

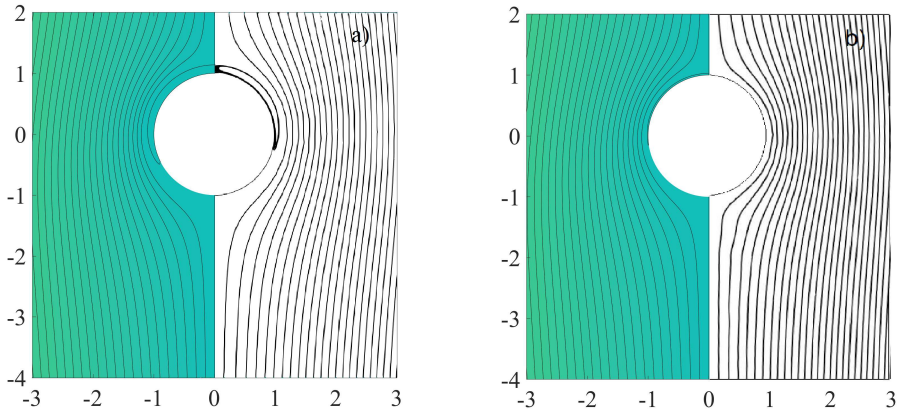


Fig. 10 Secondary flow patterns obtained analytically (left half) and numerically (right half) for (a) $\beta = 500$ and (b) $\beta = 5000$ at $\phi = 0.85$, $\gamma = 0.6$.

for the cruising speed, translational and rotational oscillation amplitudes, and phase shifts. Comparison with numerical results showed that the error in the oscillation amplitudes does not exceed 5%, in the phase shifts 0.5%, and in the cruising speed on average 6% (up to 10–15% at large amplitudes) over the entire investigated parameter range $\beta \in [500, 4000]$, $\phi \in [0.2, 0.85]$, $\gamma = 0.6$. Qualitative comparison of flow patterns confirms the correctness of the model.

5. Reproducibility. All elements of the problem statement (geometry, internal mass motion law, mechanical and hydrodynamic parameters) are fully defined. Custom classes for OpenFOAM have been developed to implement the internal mass forcing and automatic determination of the cruising speed. Configuration files, libraries, and reference data are available for use in a public GitHub repository [22]. While they are provided for OpenFOAM, the problem formulation and reference data are package-independent, making the benchmark easily portable to other CFD solvers supporting FSI calculations.

Thus, all claimed features of the proposed problem have been confirmed through numerical simulation and comparison with the analytical solution. The combination of simple geometry, complete two-way FSI coupling, bio-inspired analogy, and an analytical solution with controllable error makes the proposed benchmark a convenient tool for verification of numerical methods and debugging of FSI algorithms.

Supplementary information. Not applicable.

Acknowledgements. This research was supported by the Russian Science Foundation (project no. 22-79-10033-П).

Statements and Declarations

- **Funding** This research was supported by the Russian Science Foundation (project no. 22-79-10033-II).

- **Competing interests** The authors declare that they have no conflict of interest.
- **Ethics approval and consent to participate** Not applicable.
- **Data availability** The datasets generated during and/or analysed during the current study are available from the corresponding author on reasonable request.
- **Materials availability** Not applicable.
- **Code availability** The custom OpenFOAM libraries and case setup are available in a public repository [22].
- **Author contributions** V.D. Anisimov performed the numerical simulations and data analysis and supervised the project. A.N. Nuriev conceived the study, derived the analytical solution. O.N. Zaitseva contributed to the theoretical formulation and validation. All authors discussed the results and contributed to the final manuscript.

References

[1] Prandtl, L.: Über die Entstehung von Wirbeln in der idealen Flüssigkeit, mit Anwendung auf die Tragflügeltheorie und andere Aufgaben, pp. 18–33. Springer, Berlin, Heidelberg (1924). https://doi.org/10.1007/978-3-662-00280-3_2

[2] Birnbaum, W.: Der schlagflügelpropeller und die kleinen schwingungen elastisch befestigter tragflügel. Z. Flugtech. Motorluftschiffahrt **15**, 128–134 (1924)

[3] Theodorsen, T.: General Theory of Aerodynamic Instability and the Mechanism of Flutter. National Advisory Committee for Aeronautics, Washington, D.C. (1935). NACA R-496

[4] Garrick, I.E.: Propulsion of a Flapping and Oscillating Airfoil. National Advisory Committee for Aeronautics, Washington, D.C. (1936). NACA Report 567

[5] Lighthill, M.J.: Note on the swimming of slender fish. Journal of Fluid Mechanics **9**(2), 305–317 (1960) https://doi.org/10.1017/S0022112060001110

[6] Lighthill, M.J.: Aquatic animal propulsion of high hydromechanical efficiency. Journal of Fluid Mechanics **44**(2), 265–301 (1970) https://doi.org/10.1017/S0022112070001830

[7] Wu, T.Y.-T.: Hydromechanics of swimming propulsion. Part 1. Swimming of a two-dimensional flexible plate at variable forward speeds in an inviscid fluid. Journal of Fluid Mechanics **46**(2), 337–355 (1971) https://doi.org/10.1017/S0022112071000570

[8] Anderson, J.M., Streitlien, K., Barrett, D.S., Triantafyllou, M.S.: Oscillating foils of high propulsive efficiency. Journal of Fluid Mechanics **360**, 41–72 (1998) https://doi.org/10.1017/S0022112097008392

[9] Read, D.A., Hover, F.S., Triantafyllou, M.S.: Forces on oscillating foils for propulsion and maneuvering. Journal of Fluids and Structures **17**(1), 163–183 (2003) https://doi.org/10.1016/S0889-9746(02)00115-9

[10] Dewey, P.A., Boschitsch, B.M., Moored, K.W., Stone, H.A., Smits, A.J.: Scaling laws for the thrust production of flexible pitching panels. J. Fluid Mech. **732**, 29–46 (2013) https://doi.org/10.1017/jfm.2013.384

[11] Mivehchi, A., Dahl, J., Licht, S.: Heaving and pitching oscillating foil propulsion in ground effect. J. Fluids Struct. **63**, 174–187 (2016) https://doi.org/10.1016/j.jfluidstructs.2016.03.007

[12] Nuriev, A.N., Egorov, A.G.: Asymptotic theory of a flapping wing of a circular cross-section. Journal of Fluid Mechanics **941**, 23 (2022) https://doi.org/10.1017/jfm.2022.287

[13] Nuriev, A., Egorov, A., Zaitseva, O., Kamalutdinov, A.: Asymptotic study of the aerohydrodynamics of a flapping cylindrical wing in the high-frequency approximation. Lobachevskii Journal of Mathematics **43**, 2250–2256 (2022) https://doi.org/10.1134/S1995080222110233

[14] Egorov, A., Nuriev, A., Anisimov, V., Zaitseva, O.: Propulsive motion of an oscillating cylinder in a viscous fluid. Physics of Fluids **36**(2), 021908 (2024) https://doi.org/10.1063/5.0189346

[15] Chernous'ko, F.L.: The optimal periodic motions of a two-mass system in a resistant medium. Journal of Applied Mathematics and Mechanics **72**(2), 116–125 (2008) https://doi.org/10.1016/j.jappmathmech.2008.04.014

[16] Yegorov, A.G., Zakharova, O.S.: The energy-optimal motion of a vibration-driven robot in a resistive medium. Journal of Applied Mathematics and Mechanics **74**(4), 443–451 (2010) https://doi.org/10.1016/j.jappmathmech.2010.09.010

[17] Childress, S., Spagnolie, S.E., Tokieda, T.: A bug on a raft: Recoil locomotion in a viscous fluid. Journal of Fluid Mechanics **669**, 527–556 (2011) https://doi.org/10.1017/S002211201000515X

[18] Egorov, A., Nuriev, A., Anisimov, V.: Optimization of the movement of a cylindrical vibration-driven robot in a viscous fluid, induced by pendulum oscillations of the internal mass. Lobachevskii Journal of Mathematics **44**, 4438–4447 (2023) https://doi.org/10.1134/S1995080223100104

[19] Edelmann, J., Galdi, G.P., Karakouzian, M.M., Richter, T.: On the propulsion of a rigid body in a viscous liquid by an internal time-periodic force with a zero average. Journal of Fluid Mechanics **1032**, 39 (2026) https://doi.org/10.1017/jfm.2026.11395

[20] Stokes, G.G.: On the effect of the internal friction of fluids on the motion of pendulums. Transactions of the Cambridge Philosophical Society **9**, 8–106 (1851)

[21] Greenshields, C.: OpenFOAM v7 User Guide. https://cfd.direct/openfoam/user-guide/ Accessed 2019-10-02

[22] Nuriev, A.N., Anisimov, V.D., Zaitseva, O.N.: VR-FSI-Benchmark: A Benchmark Case for Fluid-Structure Interaction Based on a Vibration-Driven Robot. GitHub repository. https://github.com/VDAnisimov/vr-fsi-benchmark, (accessed: July 19, 2026) (2026)

[23] Triantafyllou, G.S., Triantafyllou, M.S., Grosenbaugh, M.A.: Optimal thrust development in oscillating foils with application to fish propulsion. Journal of Fluids and Structures **7**(2), 205–224 (1993) https://doi.org/10.1006/jfls.1993.1012

[24] Taylor, G.K., Nudds, R.L., Thomas, A.L.R.: Flying and swimming animals cruise at a strouhal number tuned for high power efficiency. Nature **425**, 707–711 (2003) https://doi.org/10.1038/nature02000